Continuous Monitoring of Nighttime Light Changes Based on Daily NASA's Black Marble Product Suite

Tian Li[1,*], Zhe Zhu[1], Zhuosen Wang[2, 3], Miguel O. Román[4], Virginia L. Kalb[2]

[1] Department of Natural Resources and the Environment, University of Connecticut, CT, US

[2] Terrestrial Information Systems Laboratory, NASA Goddard Space Flight Center, Greenbelt, MD, US

[3] Earth System Science Interdisciplinary Center, University of Maryland, College Park, MD, US

[4] Leidos Civil Group, Integrated Missions Operation, Reston, VA, US

* Corresponding author: Tian Li, tianli@uconn.edu

Abstract

Monitoring nighttime light (NTL) change enables us to quantitatively analyze the patterns of human footprint and socioeconomic features. NASA's Visible Infrared Imaging Radiometer Suite (VIIRS) Day/Night Band (DNB) atmospheric- and Lunar-BRDF-corrected Black Marble product provides 15-arc-second daily global nighttime radiances with high temporal consistency. However, timely and continuous monitoring of NTL changes based on the dense DNB time series is still lacking. In this study, we proposed a Viewing Zenith Angle (VZA) stratified COntinuous monitoring of Land Disturbance (COLD) algorithm (VZA-COLD) to detect NTL change at 15-arc-second resolution. Specifically, we divided the clear observations into four VZA intervals (0-20°, 20°-40°, 40°-60°, 0-60°) to mitigate the temporal variation of the NTL data caused by the combined angular effect of viewing geometry and the various kinds of surface conditions. Single term harmonic models were continuously estimated for new observations from

each VZA interval, and by comparing the model predictions with the actual DNB observations, a unified set of NTL changes can be captured continuously among the different VZA intervals. The final NTL change maps were generated after excluding the consistent dark pixels. Results show that the algorithms reduced the DNB data temporal variations caused by disparities among different viewing angles and surface conditions, and successfully detected NTL changes for six globally distributed test sites with an overall accuracy of 99.78% and a user's accuracy of 68.25%, a producer's accuracy of 66.89% for the NTL change category.

Keywords: nighttime light; change detection; time series; human activity; VZA; COLD; VIIRS; DNB; Black Marble Product

1. Introduction

Human activities are continuously changing the Earth's natural surface and the urban systems, comprising a continuum of socioeconomic and demographic phenomena. Monitoring global human footprint patterns is crucial for understanding global environmental change, sustainability, and socioeconomic status (Leu et al., 2008; Venter et al., 2016; Zhu et al., 2020). Shifts in societies, cultures, economic system structures, policies, technologies, and behaviors are rapidly affecting global ecosystems (Malecki, 1997; Ojima et al., 1994; Steffen et al., 2006). Human footprint expansion and reconstruction actions are driven by social-ecological changes, such as population growth and the consequential needs for natural resources. These drivers have modified the long-term land cover and land use features over large areas of land surfaces (Deng et al., 2009; Turner, 2010). Meanwhile, disturbance stresses caused by social shocks and behavioral changes (e.g., armed conflict and gathering events) engendered short-term changes on

the local scale (Baumann and Kuemmerle, 2016). Data-intensive frameworks for monitoring human-induced land changes at large-scale have become essential to enable a more timely, comprehensive, and deeper understanding of human activity dynamics. This demand calls for the need for reliable, timely, and large-area consistent information. In contrast to available socioeconomic and field survey data, the remote sensing nighttime light (NTL) imagery provides a reliable measure of human activity changes at the global scale with fine temporal and spatial resolutions (Jensen and Cowen, 1999; Xie and Weng, 2016).

The remotely sensed NTL data provides the direct imprint of both the spatial extent and emission intensity of the artificial light, which is a good indicator of the human footprint changes (Elvidge et al., 1997; Levin et al., 2020; Zhang and Seto, 2011). Characteristics of artificial nocturnal illumination are often associated with the economic and demographic structures of modern society (Green et al., 2015). The artificial NTL intensity is strongly responded to the growth or decrease of the health and development of the society (Hölker et al., 2010). Strong correlations have been found among the NTL trends and socioeconomic status (Ma et al., 2012), which enables us to estimate the spatial-temporal dynamics of society based on the NTL changes. Accurate results have been produced by using the NTL datasets as the major inputs for mapping the urbanization processes (Shi et al., 2014), estimating Gross Domestic Product (GDP) and mapping poverty (Yu et al., 2015), monitoring natural hazards and recurrent disaster impacts on underserved communities (Machlis et al., 2022; Román et al., 2019), armed conflicts (Li et al., 2018), cultural behaviors (Liu et al., 2019; Román and Stokes, 2015), and detecting long-term landscape changes in the urbanized regions (Chen et al., 2019).

Compared with the previous Defense Meteorological Satellite Program's Operational Line Scanner (DMSP/OLS) sensor, the Visible Infrared Imaging Radiometer Suite (VIIRS) Day/Night Band (DNB) provides higher spatial resolution NTL data with significant improvement in its quality, traceability, and consistency (Elvidge et al., 2017). However, high uncertainties caused by both the dynamics of the emission sources and the environmental impacts still exist in the VIIRS DNB observations (Coesfeld et al., 2018; Elvidge et al., 2022; Li et al., 2020; Wang et al., 2021) which makes time series analysis (e.g., daily) of DNB observations extremely challenging. Moreover, the VIIRS DNB observations are inevitably subject to the extraneous impacts of the angular effects, surface BRDF and albedo, lunar phases, atmospheric effects, cloud and snow contamination, and vegetation canopy (Wang et al., 2021). To alleviate the significant variation caused by the external effects, previous studies used the monthly or annual composited NTL data to smooth the variation (Elvidge et al., 2021; Levin, 2017; Liu et al., 2019; Yang et al., 2020), which is a viable solution but also significantly reduces the data temporal frequencies, making it difficult to provide timely information and monitor short-term changes (Xie et al., 2019; Zhao et al., 2020; Zheng et al., 2021).

NASA's Lunar-BRDF-corrected Black Marble NTL product (VNP46A2) provides daily 15-arc-second spatial resolution Visible Infrared Imaging Radiometer Suite (VIIRS) Day/Night Band (DNB) data with operational correction for the lunar phase effects (Román et al., 2018). Significant reduction of the temporal variation has been achieved with the correction of the major sources of noise from the lunar cycle (Elvidge et al., 2022; Wang et al., 2021) which provides new opportunities for analyzing NTL dynamics based on the daily DNB data for the first time. However, there are still some remaining factors that could cause large variations in

NASA's Black Marble products, such as cloud and snow missed in the Quality Assurance (QA) flag (Wang et al., 2021), vegetation phenology, surface albedo (Levin, 2017; Tang et al., 2021), and angular effect from the illuminating artificial lights (Li et al., 2022; Tan et al., 2022), which makes their direct usage for time series analysis difficult.

In this study, we aimed to develop a new algorithm for continuous monitoring of NTL changes based on daily VIIRS DNB observations from NASA's Black Marble standard product suite, which adds robustness to the large variation caused by cloud and cloud shadow missed in the Level 3 QA flagging process, vegetation phenology, snow, and angular effects introduced by illuminating artificial lights.

2. Study Area and Data

We selected eight globally distributed regions from different land cover and land use types, and urban development transitions, corresponding to various NASA Black Marble Level-3 VIIRS tiles (latitude/longitude extent of 10°×10° per tile): h10v04, h13v11, h18v04, h17v08, h29v05, h32v12, h11v07, and h21v05 (Fig. 1). The analysis employed all available 15-arc-second spatial resolution daily DNB atmospheric- and Lunar-BRDF-corrected and Top of Atmosphere (TOA) Black Marble NTL radiance collected between 2013 and 2020.

We also manually interpreted 610 calibration samples that have undergone various kinds of changes, such as construction actions, economic growth, gathering events, armed conflict, power outages, and new streetlights, as well as stable samples without any NTL changes, based on the opportunistic strategy around the major cities and metropolitan areas within the study area (Table

1). To explore the complex angular effects, the calibration samples were selected from areas with typical types of local geometry conditions, such as downtown areas with skyscrapers, single- and multi-story residential regions, and areas with dense vegetation canopy. For each calibration sample, we recorded the interval of each change event for the period between 2013 and 2020. Note that certain NTL changes, such as transition changes, defined as changes in long-term trend, can last for more than a year.

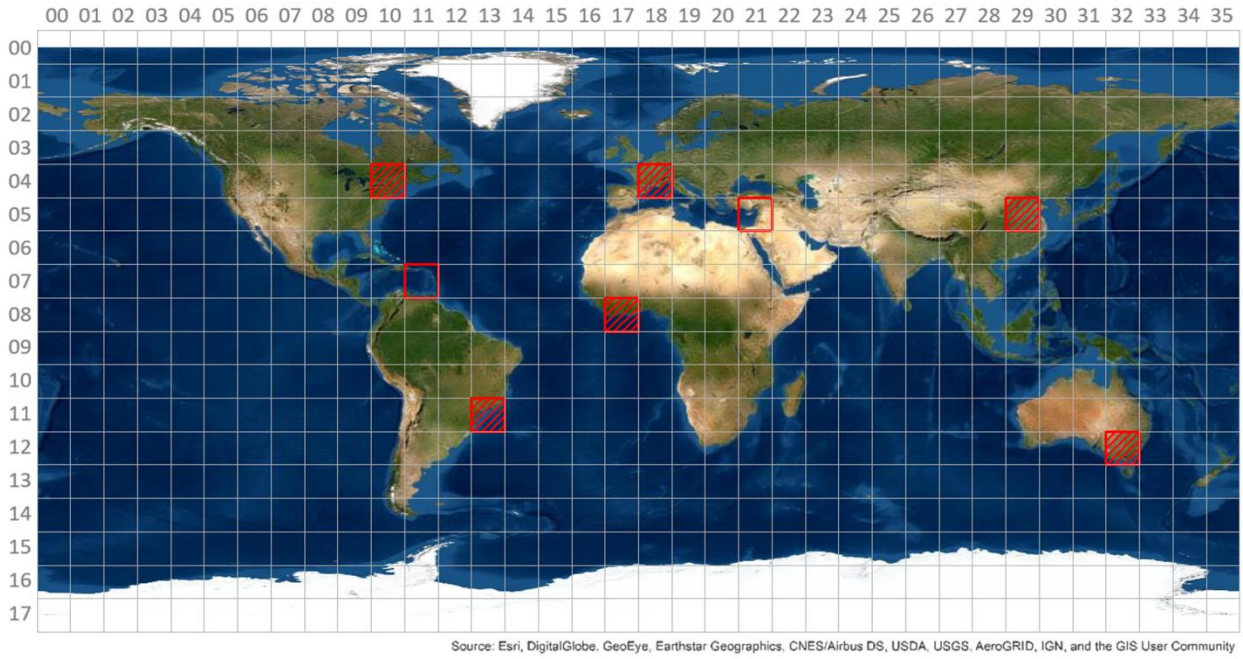

Fig. 1. Eight VIIRS linear latitude/longitude 10°×10° tiles in this study. The calibration samples were collected from all eight tiles with red squares, and the validation samples were collected from the six titles with red stripes. The numbers of the rows and columns represent the "horizontal" and "vertical" number of the tiles, respectively. The background is the Esri ArcMap World image.

Table 1. Calibration samples and their corresponding regions of interest.

Tile ID	Tile Name	Country/Region	Major Cities	Number of Samples (Pixels)
1	h10v04	U.S.	New York; Boston	78
2	h13v11	Brazil	Rio de Janeiro	82
3	h18v04	Italy	Milan	70
4	h17v08	Ivory Coast	Abidjan	74
5	h29v05	China	Beijing; Baoding;	74
6	h32v12	Australia	Melbourne	70
7	h11v07	Puerto Rico	San Juan	74
8	h21v05	Egypt; Israel; Syria	Cairo; Netanya; Aleppo	88

3. Methods

We proposed an algorithm called "View Zenith Angle (VZA) Stratified COLD" (hereafter referred to as VZA-COLD), which is built on the Landsat-based COntinuous monitoring of Land Disturbance (COLD) algorithm (Zhu et al., 2020). It includes three major innovations that are: (i) cloud/snow buffer; (ii) change detection based on observations from four stratifications of VZA; and (iii) consistent dark pixel (DNB radiance < 1.0 $nW * m^{-2} * sr^{-1}$) removal. The workflow of the VZA-COLD algorithm is illustrated in Fig. 2. The first component involved removing the remaining cloud and snow observations based on the exclusion of cloud and snow edge pixels that are partially influenced by clouds or snow. In the second component, DNB observations were stratified into four groups based on the VZA intervals to mitigate the variance caused by the compounded impacts from the different viewing geometry and surface condition, and thus, reduce the overall time-series variation. For each VZA interval, NTL changes were monitored based on the change detection framework similar to the COLD algorithm to obtain the individual sets of estimated time series models and detect a unified set of breakpoints among all the VZA

intervals continuously. The third component involved filtering the consistent dark pixels with a minimum detectable NTL radiance threshold. The VZA-COLD algorithm was calibrated based on the calibration samples, in which the changes detected within the period of ± six months of the calibration sample change intervals were determined as the right call. Metrics of omission rates, commission rates, and F1 score of NTL change were used to evaluate algorithm performance. The final map accuracy was evaluated based on independent validation samples following the "good practice" protocols (Olofsson et al., 2014).

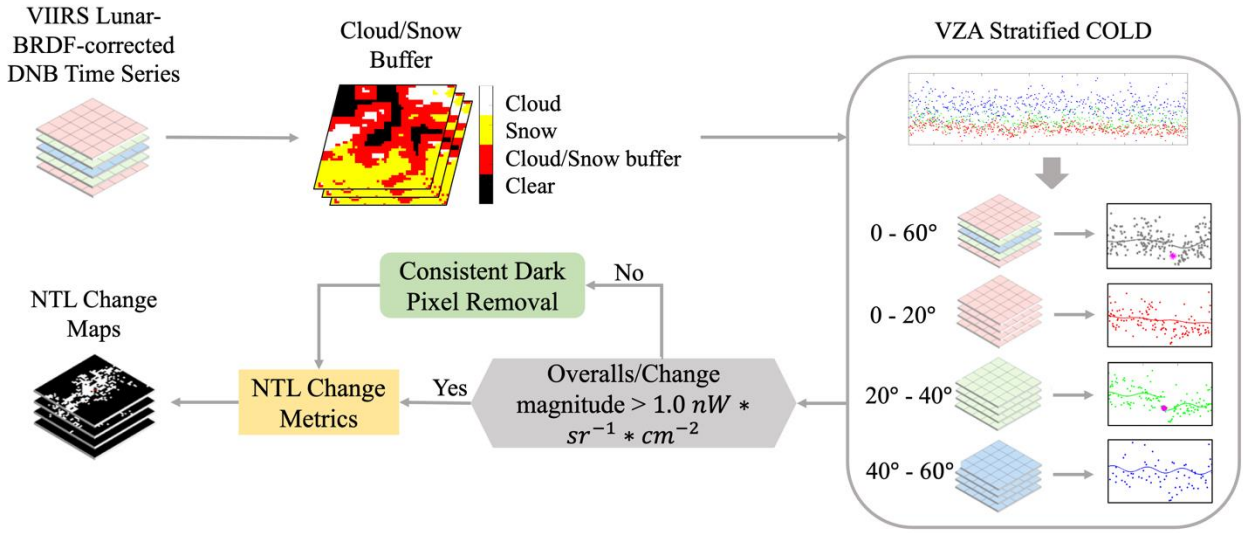

Fig. 2. Flowchart of the VZA-COLD algorithm. NTL: nighttime light; VZA: View Zenith Angle; COLD: COntinuous monitoring of Land Disturbance; DNB: Day/Night Band; BRDF: Bidirectional Reflectance Distribution Function.

3.1. Remove remaining cloud and snow impacted observations

Considering that cloud and snow edge pixels are very likely to be influenced by thin clouds and snow, a spatial buffer was applied to remove these edge pixels. Confident/probable cloud, cirrus cloud, snow/ice, and observations were firstly removed according to the QA flags of the standard NASA's Black Marble product. The cloud/snow edge pixels removal was tested by dilating

cloud/snow pixels (at 8-connected directions) from 0 to 11 pixels to find the optimal moving window size based on our calibration samples. For the moving window size equal to or less than five pixels, both omission and commission errors dropped gradually along with the increase of the window sizes (Fig. 3a). A decrease in F1 scores and an increase in omission/commission errors were observed when the moving window size was larger than five pixels (Fig. 3a), which is mostly due to the removal of too many clear observations for change detection. Thus, the 5x5 pixel moving window was selected as the optimal buffer size for masking potential cloud/snow-influenced pixels. Fig. 3b shows the cloud/snow masks and their 5x5 pixel buffer for an example image collected at tile h10v04 on Day-of-Year (DOY) 45 in 2015, in which the red pixels are the ones that were captured by the cloud/snow buffer.

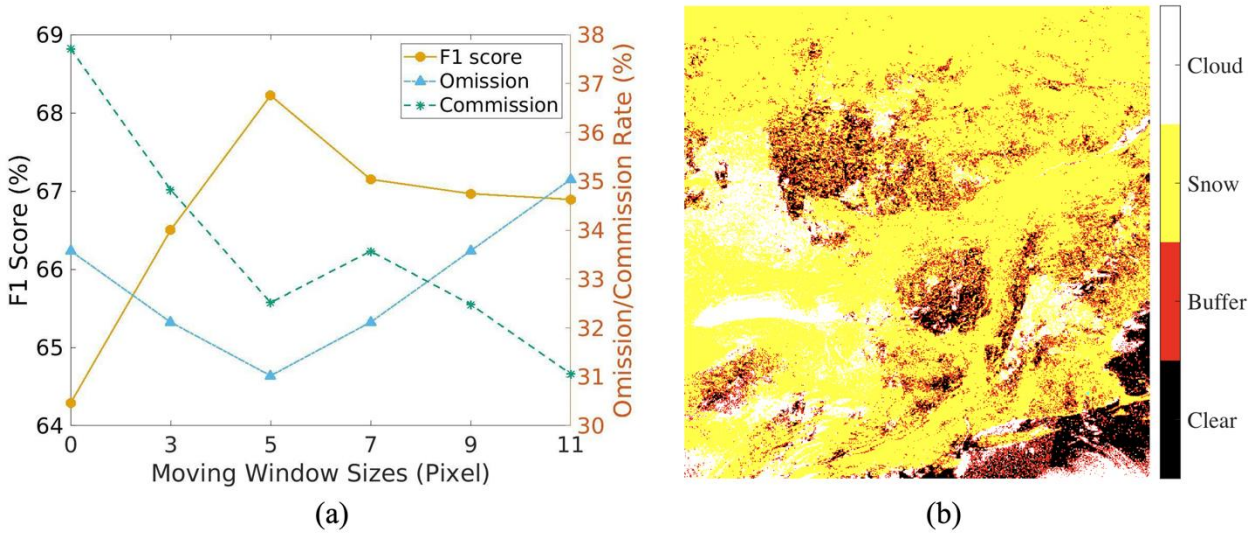

(a) (b)

Fig. 3. Analysis of optimal buffer size for cloud/snow removal. (a) Calibration accuracies for the cloud/snow buffer with different moving window sizes. (b) The cloud/snow mask with 5x5 pixel buffer for a NASA Lunar-BRDF-corrected Black Marble product output (VNP46A2) from tile h10v04 on day-of-year 45 in 2015.

3.2. Viewing zenith angle stratification

The DNB observations were grouped into four VZA intervals, 0-20°, 20°-40°, 40°-60°, and 0-60°, to mitigate the angular effect. Some pixels have uniform DNB values among different VZA ranges, while others have uneven DNB magnitudes and large variations across the VZA (e.g., Fig 4). This VZA-related DNB radiance disparity is mainly caused by the complex and case-by-case joint angular effects of their viewing angle and local geometry (Li et al., 2019a; Tan et al., 2022; Wang et al., 2021). For low building and open area pixels with streetlights fully shielded, such as rural settlements without adjacent occlusions (Fig. 4a), almost no differences in the DNB value were observed among different VZA. While significant VZA interval related disparities were observed in areas with multiple story buildings and rural settlements surrounded by dense tree canopy (Fig. 4b-c). In downtown areas with skyscrapers, near-nadir observations have the largest overall radiance and variations (Fig. 4b). In the dense residential areas, however, the off-nadir DNB radiances are dramatically larger than the ones with lower VZA values (Fig 4c). This inconsistency of the DNB radiances consequently led to inequalities in the sensitivity of monitoring NTL changes, therefore disparities in the occurrences, magnitude, and timing of the changes across the VZA. Fig. 5 shows a sample with disparate magnitudes and occurrences of DNB radiance change among the different VZA ranges. The near-nadir time series has a larger magnitude of change in early 2016 than the ones with 20°-40° VZA, while this 2016 change is hardly noticeable from the off-nadir time series with 40°-60° VZA (Fig 5). Thus, to enhance the temporal consistency for angular affected NTL emission areas, we divided the VZA range into three equal ranges, 0-20°, 20°-40°, and 40°-60°, following the near-nadir (0-20°) and off-nadir (40°-60°) divisions of the NASA's Black Marble product. A fourth VZA interval of 0-60° is also included to balance the trade-off between DNB time series temporal consistency and temporal

density, as time series observations stratified by VZA will substantially reduce the data temporal density and therefore reduce their capability in monitoring NTL changes that can be only observed for a very short time (e.g., loss of electric grid power supply or large-scale gathering events).

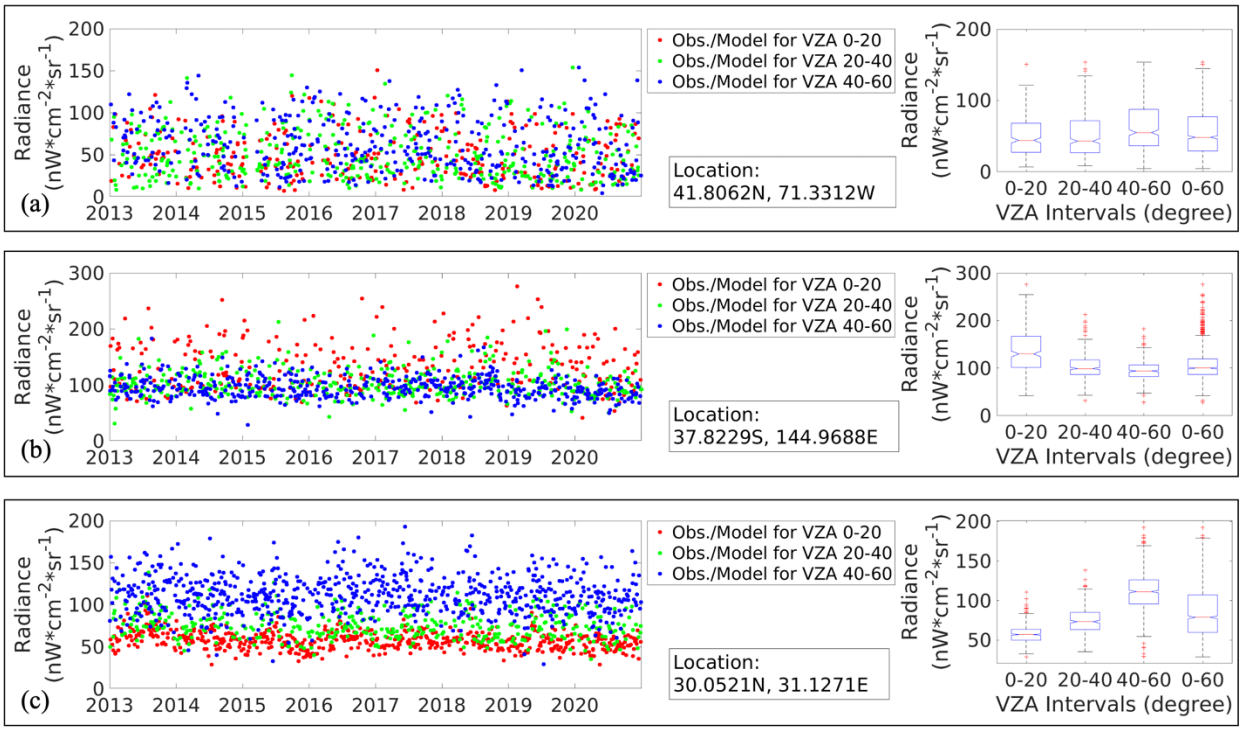

Fig. 4. The VZA stratified DNB time series (left) and the boxplot of DNB observations of different VZA intervals (right) for the corresponding pixel on the left. The red, green, and blue dots indicate the DNB observations within different VZA intervals. (a) A rural grocery store in Seekonk, MA, U.S.; (b) Downtown Melbourne, Australia; (c) Dense residential area with multi-story buildings, Nahyan, Egypt.

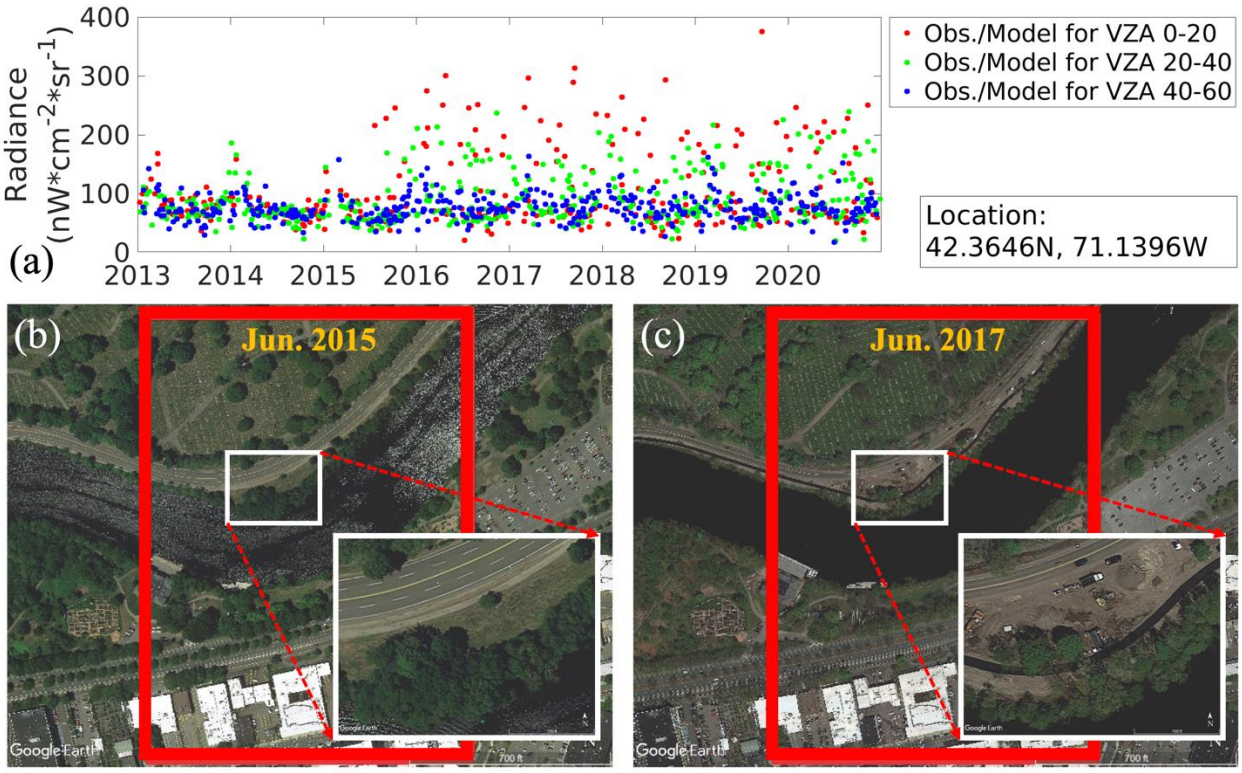

Fig. 5. The VZA stratified DNB time series and high-resolution images of a riverside esplanade with new pedestrians built in 2016 near Charles River in Massachusetts, U.S. (a) DNB time series at the riverside esplana. The red, green, and blue dots indicate the DNB observations within different VZA intervals. (b) The high-resolution Google Earth image in June 2015 of the selected pixel in Fig. 5a. The red rectangle represents the location and size of the selected pixel. (c) The high-resolution Google Earth image in June 2017 of the selected pixel in Fig. 5a. The red rectangle represents the location and size of the selected pixel.

3.3. Continuous monitoring of NTL change

The VZA-COLD algorithms were applied to estimate time series models from DNB observations collected within different VZA intervals while collectively identifying NTL changes across all VZA strata. For DNB observations stratified within each VZA interval, an individual harmonic model was estimated to capture the seasonality and trend of the DNB time series, which could greatly reduce the impact from the intra-annual (e.g., vegetation phenology and snow) and inter-annual (e.g., gradual economic growth and vegetation long-term growth) changes. We tested the models with unimodal, bimodal, and trimodal seasonality (4, 6, and 8 coefficients) based on the

Ordinary Least Square (OLS) regression, Least Absolute Shrinkage and Selection Operator (LASSO) regression (Tibshiranit, 1996), and robust regression (Hampel et al., 2011; Zhu et al., 2012) to explore the optimal combinations for modeling the daily DNB time series. We observed that models with a single-term harmonics model (Eq. 1) and based on robust regression had the best results for our calibration samples and were more robust to outliers and less likely to be overfitted. Therefore, the single-term harmonic model (Eq. 1) estimated based on robust regression was selected to predict the overall DNB magnitude, intra-annual seasonality, and inter-annual trends, which would be used in continuous monitoring of NTL changes.

$$\hat{\rho}_{i,x} = a_0 + a_1 cos\left(\frac{2\pi}{T}x\right) + b_1 sin\left(\frac{2\pi}{T}x\right) + c_1 x \quad (1)$$

where,

$\hat{\rho}_{i,x}$: Predicted DNB value for the *i*th VZA interval at Julian date *x*.

x: Julian date.

T: Number of days per year (T = 365.25).

a_0: Coefficient for overall value for the DNB.

a_1, b_1: Coefficient for intra-annual change for the DNB.

c_1: Coefficient for inter-annual change (slope) for the DNB.

Continuous change detection was conducted based on the models estimated from each VZA stratification following the COLD algorithms (Zhu et al., 2020), by comparing the actual observations with the model predictions. Breakpoints were identified based on the number of consecutive anomaly observations beyond the applied change probability thresholds. The VZA-COLD made three major changes compared with the original COLD algorithm. First, due to the high temporal frequency and the large fluctuations observed with the daily DNB time series,

VZA-COLD would tolerate one of the observations (except for the first one) not showing up as an anomaly in the consecutive anomaly test. Second, VZA-COLD detected changes based on a set of four time series models estimated from observations of different VZA intervals (instead of observations from different spectral bands), and when a breakpoint was identified by any of the VZA interval models, it would be applied to all the four VZA-stratified models, and thus, dividing their time segments with the same break time. Third, the optimal parameters for the change detection process were also different from the default COLD algorithm. We tested the number of consecutive anomaly observations to confirm a change from 12 to 16, along with the change probabilities of 70%, 75%, 80%, 85%, and 90%, and analyzed the performance metrics of omission rate, commission rate, and F1 score based on the calibration samples (Fig. 6). According to the results, the consecutive anomaly observation of 14 and 75% change probability were selected to detect NTL changes.

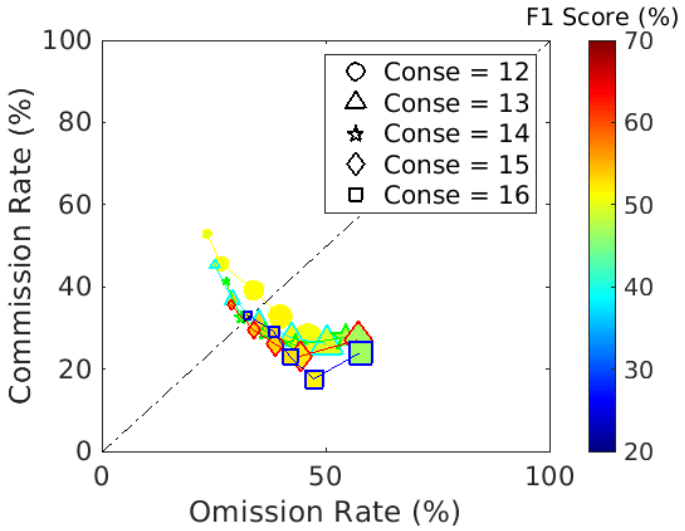

Fig. 6. Change detection results with different numbers of consecutive anomaly observations, and different change probabilities. Where the shapes of the marker represent the selected number of consecutive anomaly observations (from 12 to 16), the marker sizes indicate the applied change probability (70%, 75%, 80%, 85%, and 90%), and the marker face colors show the F1 scores.

3.4. Consistent dark pixel removal

Change probability in VZA-COLD was normalized by the RMSE calculated from robust regression, which could be still sensitive to pixels that are consistently dark due to their relatively low temporal uncertainties and resulted very small RMSE values in model estimation. Therefore, a slight change in the DNB values caused by outliers could lead to a substantial increase in the final normalized change probability, and result in commission errors. To mitigate this issue, the detected breakpoints with low overall values of DNB and small change magnitudes are considered as low confidence changes that are more likely to be commission errors caused by the outliers. Changes detected over the consistent dark area were identified based on the model predicted overall DNB values before and after the change, and the corresponding change magnitude. A threshold of 1.0 $nW * m^{-2} * sr^{-1}$, which is two times the breakthrough value of the NTL detection limit ($L_{min} = 0.5\ nW * m^{-2} * sr^{-1}$) defined in the daily Black Marble product (Román et al., 2018), was applied to exclude the low confidence changes in consistent dark areas. The detected breakpoints, with before-break overall value, after-break overall value, and change magnitude value all less than 1.0 $nW * m^{-2} * sr^{-1}$, would be identified as consistent dark pixels and would be removed from the final change detection results. Commissions caused by the scattering light (Fig. 7) and salt-and-pepper noise (Fig. 8) were substantially removed by this approach.

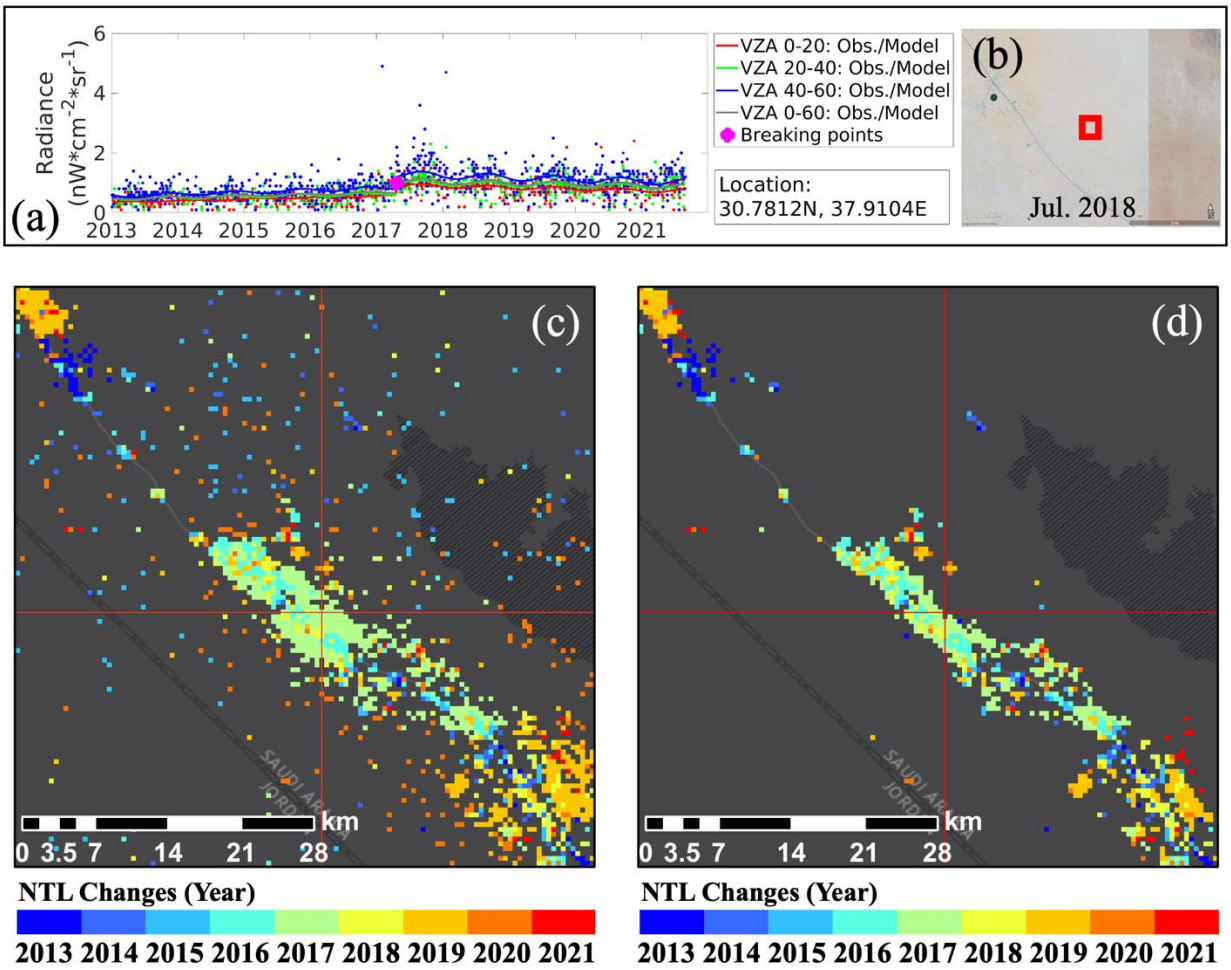

Fig. 7. DNB time series, high-resolution image, and annual NTL change maps for the selected consistent dark pixel with scattering light. It is located near a desert highway with improvement in electrification around 2017, in northwestern Saudi Arabia. (a) DNB time series at a dark barren pixel with a commission error before the consistent dark pixel removal was applied. The red, green, blue, and grey colors indicate the different VZA intervals, lines represent the fitting models, small dots are the DNB observations, and the large magenta dot is the detected change (red cross in Fig. 7c) that would be excluded by the dark pixel removal process (red cross in Fig. 7d). (b) The high-resolution Google Earth image in July 2018 of the selected pixel in Fig. 7a. The red rectangle represents the location and size of the selected pixel. (c) The accumulated annual NTL change maps before the dark pixel removal process. (d) The accumulated annual NTL change maps after the dark pixel removal process. The dark background in Fig. 7c and Fig. 7d is the Esri ArcMap Dark Gray Canvas base map.

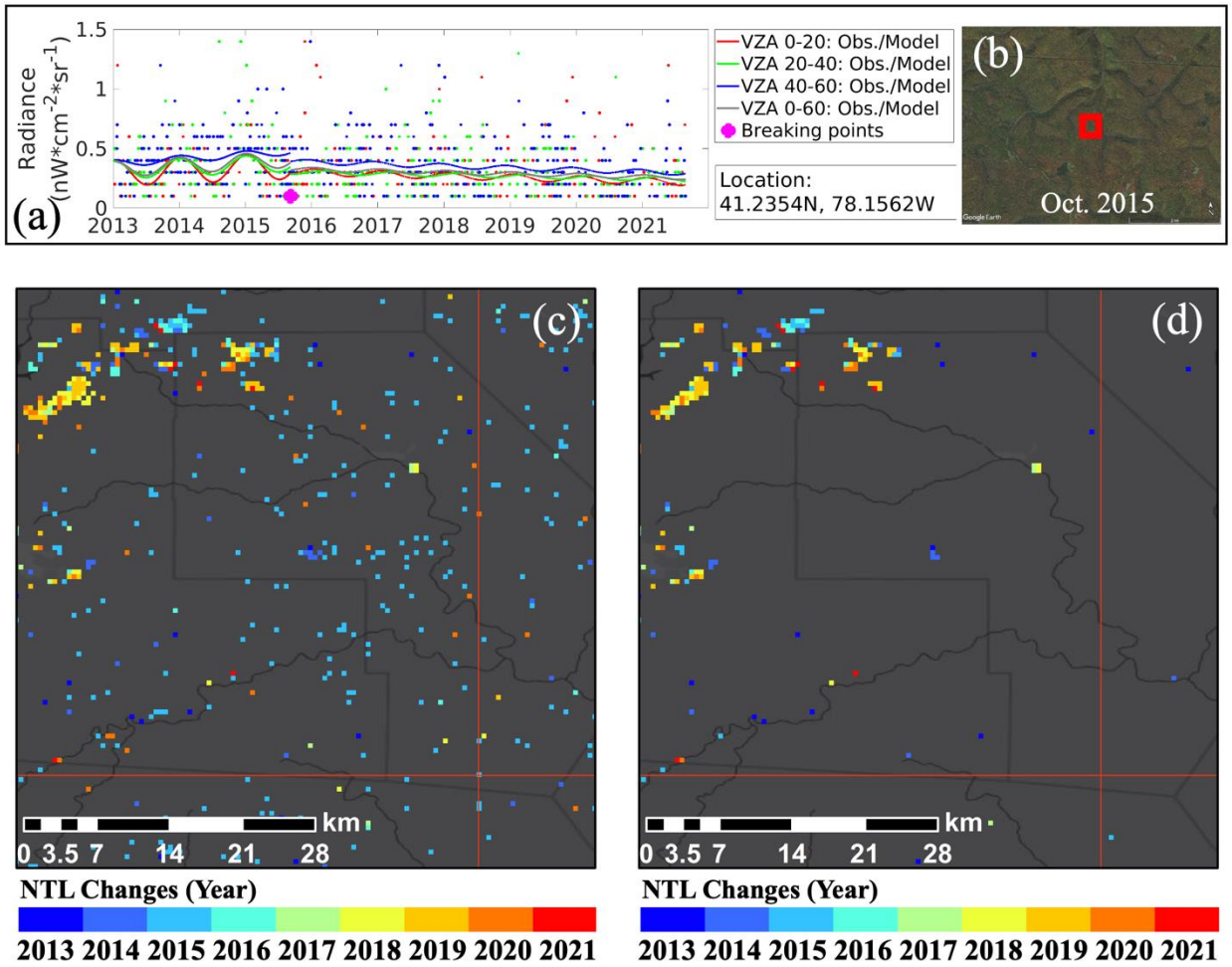

Fig. 8. DNB time series, high-resolution image, and annual NTL change maps of the selected consistent dark pixel with pepper-and-salt noise. It is located in the vegetation areas of Mifflin, PA, US. (a) The DNB time series of a selected pixel with a commission error before the consistent dark pixel removal was applied. The red, green, blue, and grey colors indicate the different VZA intervals, lines represent the estimated models, small dots are the DNB observations, and the large magenta dot is the detected change (red cross in Fig. 8c) which would be excluded by the dark pixel removal (red cross in Fig. 8d). (b) The high-resolution Google Earth image in October 2015 of the selected barren pixel. The red rectangle represents the location and size of the selected pixel. (c) The accumulated annual NTL change maps before the dark pixel removal. (d) The accumulated annual NTL change maps after the dark pixel removal. The dark background in Fig. 8c and Fig. 8d is the Esri ArcMap Dark Gray Canvas base map.

3.5. Accuracy assessment

A total of six VIIRS tiles, including h10v04, h13v11, h18v04, h17v08, h29v05, and h32v12, were selected as the validation tiles to cover all six non-polar continents (Fig. 1). The stratified random sampling strategy (Olofsson et al., 2014) was applied for selecting the validation

samples. The annual change maps from 2013 and 2021 of all the validation tiles were used for the stratification, and a total number of 1,088 samples, of which 931 from the stable stratum and 157 from the change stratum were selected. Each reference sample represents not only a location on the ground but also a place in time. Manual interpretation of the validation samples was conducted based on original NTL imagery, high-resolution images from Google Earth and PlanetScope data, International Space Station (ISS) nighttime photos, and other available socioeconomic data. A reference sample will be labeled as correct if the mapped category (e.g., change or stable) is the same as it is interpreted in the selected calendar year.

4. Results

4.1. Visual assessment

We applied the VZA-COLD algorithm to all the selected tiles (Fig. 1) to examine its change detection performances for various kinds of human-related NTL changes over different regions. The annual and day-of-year NTL change maps from 2013 to 2021 were created for every pixel. To demonstrate the algorithm's abilities in monitoring NTL changes, we investigated a range of urban and peri-urban regions with human activity changes corresponding to different land use, demographic, and socioeconomic typologies (Stokes and Seto, 2019). The results, shown in Figs. 9-16, illustrated how the algorithm can accurately capture NTL changes caused by the major types of both short-term and long-term transitions. These factors include, but are not limited to, urbanization processes in sub-urban areas, non-residential constructions of public facilities, land cultivation of a new modern agriculture field, redevelopment of a pre-existing urban area triggered by the economic growth, de-electrification derived by the renovation of lighting technologies and environmental policies, armed conflicts, and power grid loss caused by natural

hazards. Meanwhile, the identified changed areas covered a wide range of human footprints with different land cover and land use types, including the highly populated urban areas, urban green space, suburban and rural areas, agricultural fields, roads, and barren land regions with human activities.

Urbanization with constructions of residential and non-residential developments is one of the most prevalent human-driven land cover and land use changes. Fig. 9 showed the urban expansion process of a new residential community in the suburban area of Melbourne, Australia that converted the agriculture fields to impervious surfaces. A gradual NTL change was captured by the algorithm at this site, which is consistent with the built-up period of this new settlement from 2017 to 2021 (Fig. 9c). Figs. 10-11 showed the construction actions of a newly built international airport in the suburban areas of Beijing, China (Fig. 10) and the Olympic Parks in Rio de Janeiro, Brazil (Fig. 11). Multiple NTL changes were identified for the new international airport, which aligned well with the different construction stages (Fig. 10c). The timing of these three identified changes agreed with the start of land clearance in February 2016, the time when the major construction of the airport was finished in 2018, and its opening date in September 2019. At the Olympic Parks in Rio, an increase in artificial light emissions was caused by the new facilities and the large gathering event of the Olympic Games in summer 2016, and this abrupt NTL change was also successfully captured (Fig. 11). In addition to urban developments, the land cultivation engendered by the food consumption in agricultural land can also be captured by the DNB time series. Fig. 12 showed a new modern organic vegetable greenhouse built with LED plant light at night in the low light area of Canada. According to the time series result of the selected pixel (Fig. 12c), a dramatic increase of the NTL was captured in 2017 after

the greenhouse was put into use. Redevelopment driven by the population and economic growth, and de-electrification caused by new technologies and environmental policies can shift intensities of the artificial NTL over pre-existing developments without land conversions. Fig. 13 showed the redevelopment of urban areas in Abidjan, Ivory Coast. Foreign investments promoted both GDP and population density of the urban environment of Abidjan (Ramiaramanana et al., 2021), which was detected in 2014. The large-scale renovation of LED streetlights in the suburban areas of Milan that were planned by environmental policies encouraged by the International Registered Exhibition in 2015 (World EXPO) can also be detected from the annual NTL change map (Fig. 14). A significant drop in the NTL radiances was captured in 2014 after the new energy-saving LED streetlights with less upward emission were installed.

Changes in human behavior at night, armed conflict, and power grid loss can lead to short-term NTL shifts. VZA-COLD successfully detected these short-term changes in a timely manner. In urban areas with high dynamics of NTL caused by armed conflicts such as the Syrian Civil War in Raqqa, the algorithm identified multiple NTL changes between the stable periods with relatively short durations (Fig. 15). In September 2017, Puerto Rico was hit by two powerful hurricanes, and the abrupt power outage and gradual restoration were successfully identified by the VZA-COLD algorithm (Fig. 16).

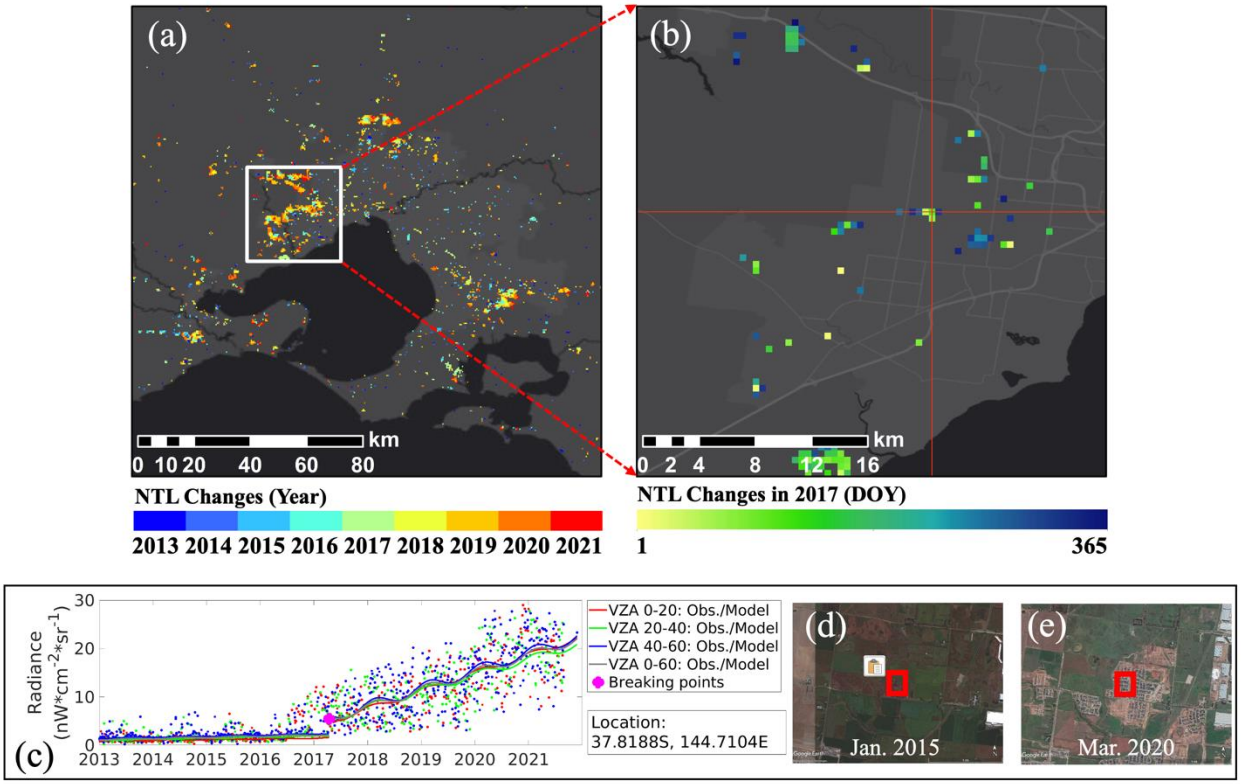

Fig. 9. The NTL change maps, the time series plot of a selected pixel, and high-resolution images for an urbanized suburban area in Melbourne, Australia. (a) The accumulated annual NTL change maps from 2013 to 2021 with the latest detected change year presented. (b) The day-of-year NTL change maps over the region enlarged from the white rectangle from Fig. 9a. (c) The time series plot of a selected pixel (red cross in Fig. 9b) and the corresponding VZA-COLD detection results, in which the red, green, blue, and grey colors indicate the different VZA intervals, lines represent the estimated models, small dots are the DNB observations, and the large magenta dot is the detected change. (d) The high-resolution Google Earth image in January 2015. The red rectangle represents the location and size of the selected pixel. (e) The high-resolution Google Earth image in March 2020. The red rectangle represents the location and size of the selected pixel. The dark background in Fig. 9a and Fig. 9b is the Esri ArcMap Dark Gray Canvas base map.

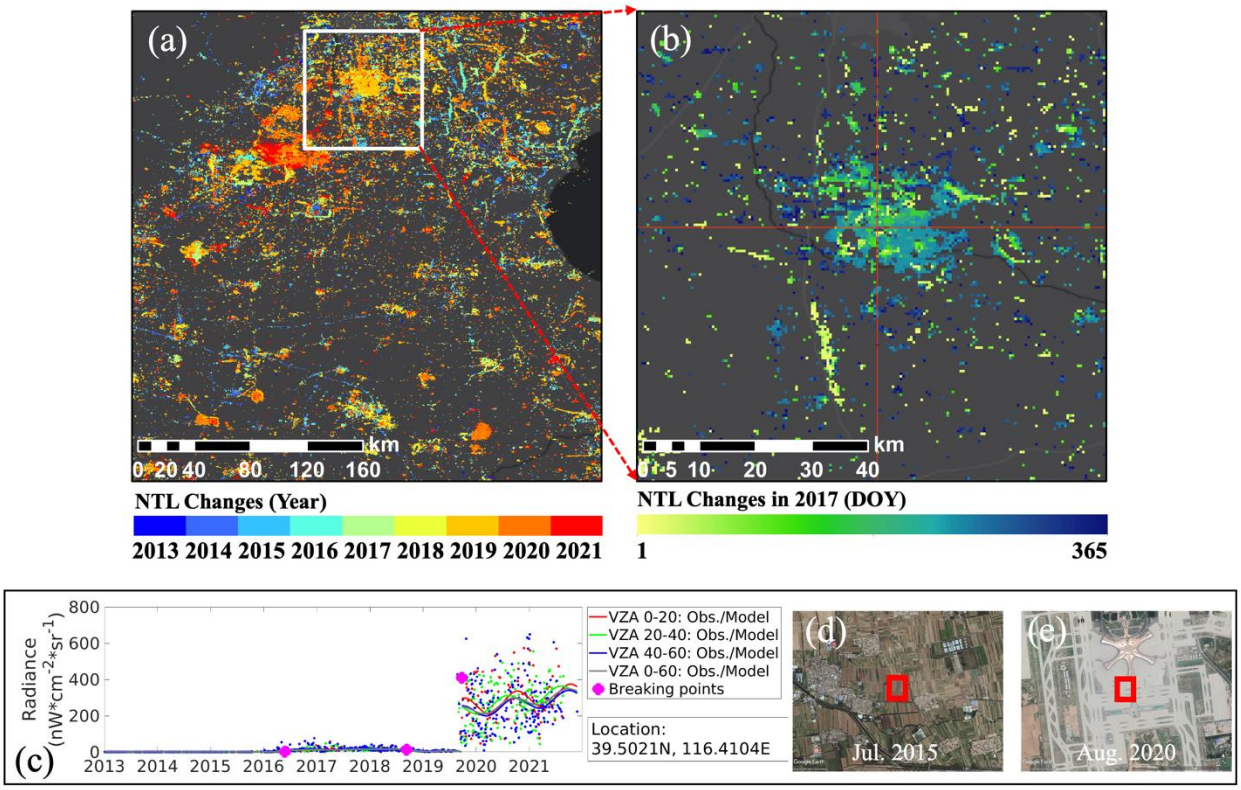

Fig. 10. The NTL change maps, the time series plot of a selected pixel, and high-resolution images for a new airport built in Beijing, China. (a) The accumulated annual NTL change maps from 2013 to 2021 with the latest detected change year presented. (b) The day-of-year NTL change map in 2019 over the region enlarged from the white rectangle from Fig. 10a. (c) The time series plot of a selected pixel (red cross in Fig. 10b) and the corresponding VZA-COLD detection results, in which the red, green, blue, and grey colors indicate the different VZA intervals, lines represent the estimated models, small dots are the DNB observations, and the large magenta dots are the detected changes. (d) The high-resolution Google Earth image in January 2015. The red rectangle represents the location and size of the selected pixel. (e) The high-resolution Google Earth image in August 2020. The red rectangle represents the location and size of the selected pixel. The dark background in Fig. 10a and Fig. 10b is the Esri ArcMap Dark Gray Canvas base map.

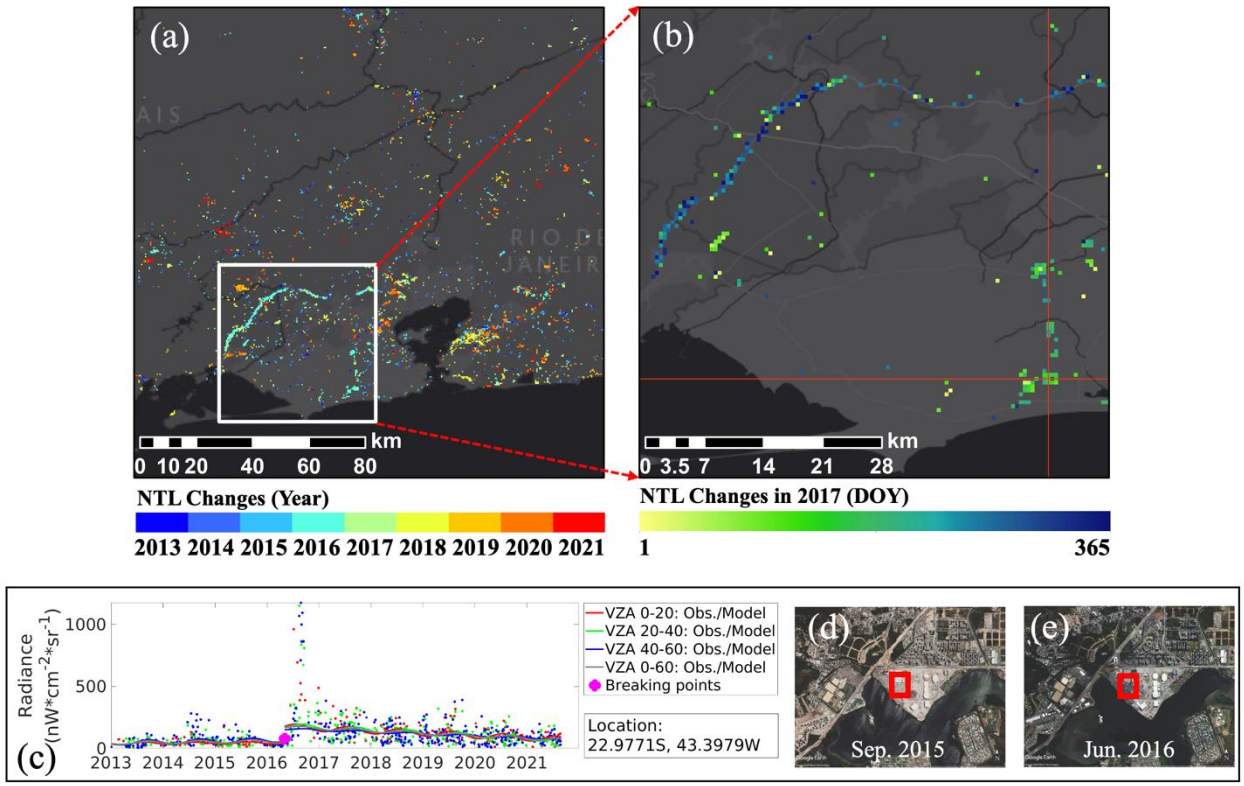

Fig. 11. The NTL change maps, the time series plot of a selected pixel, and high-resolution images for the Olympic Park in Rio, Brazil. (a) The accumulated annual NTL change maps from 2013 to 2021 with the latest detected change year presented. (b) The day-of-year NTL change map in 2016 over the region enlarged from the white rectangle from Fig. 11a. (c) The time series plot of a selected pixel (red cross in Fig. 11b) and the corresponding VZA-COLD detection results, in which the red, green, blue, and grey colors indicate the different VZA intervals, lines represent the estimated models, small dots are DNB observations, and the large magenta dot is the detected changes. (d) The high-resolution Google Earth image in September 2015. The red rectangle represents the location and size of the selected pixel. (e) The high-resolution Google Earth image in June 2016. The red rectangle represents the location and size of the selected pixel. The dark background in Fig. 11a and Fig. 11b is the Esri ArcMap Dark Gray Canvas base map.

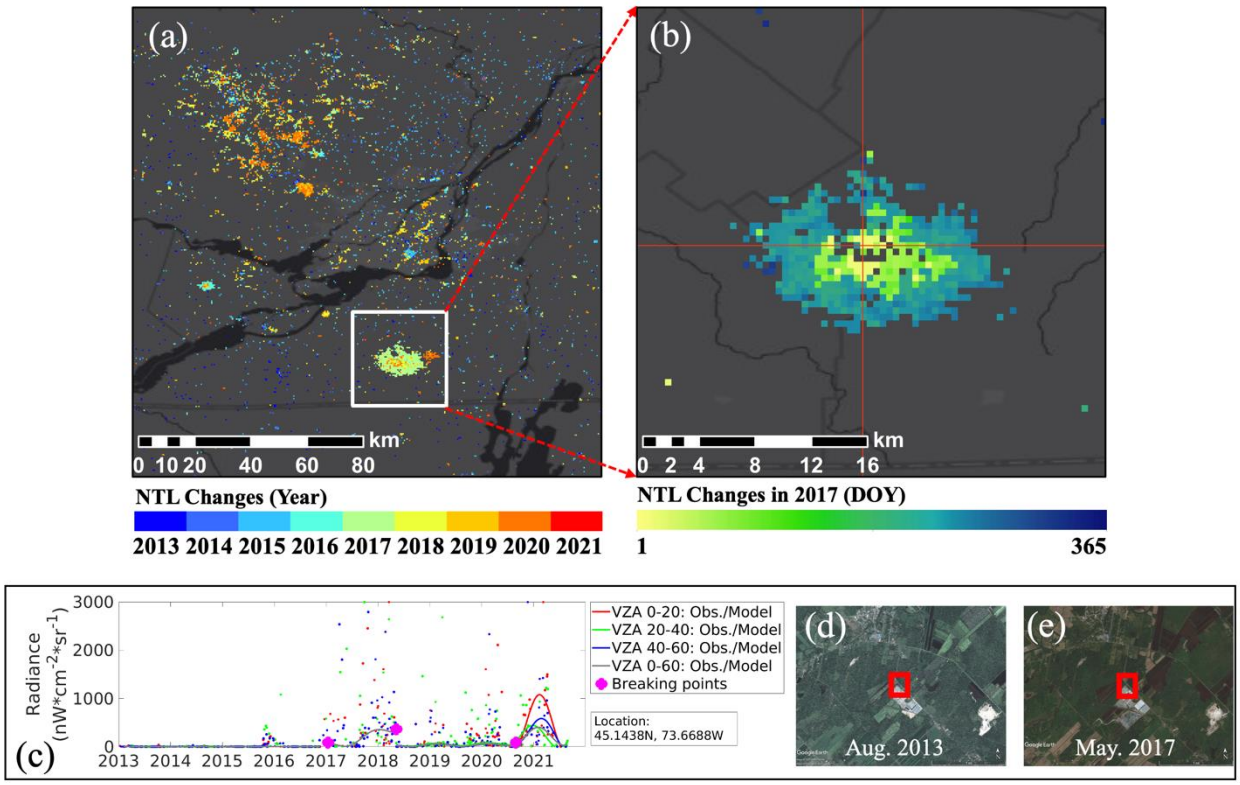

Fig. 12. The NTL change maps, the time series plot of a selected pixel, and high-resolution images for a new organic vegetable greenhouse built in Canada. (a) The accumulated annual NTL change maps from 2013 to 2021 with the latest detected change year presented. (b) The day-of-year NTL change map in 2017 over the region enlarged from the white rectangle from Fig. 12a. (c) The time series plot of a selected pixel (red cross in Fig. 12b) and the corresponding VZA-COLD detection results, in which the red, green, blue, and grey colors indicate the different VZA intervals, lines represent the estimated models, small dots are the DNB observations, and the large magenta dots are the detected changes. (d) The high-resolution Google Earth image in August 2013. The red rectangle represents the location and size of the selected pixel. (e) The high-resolution Google Earth image in May 2017. The red rectangle represents the location and size of the selected pixel. The dark background in Fig. 12a and Fig. 12b is the Esri ArcMap Dark Gray Canvas base map.

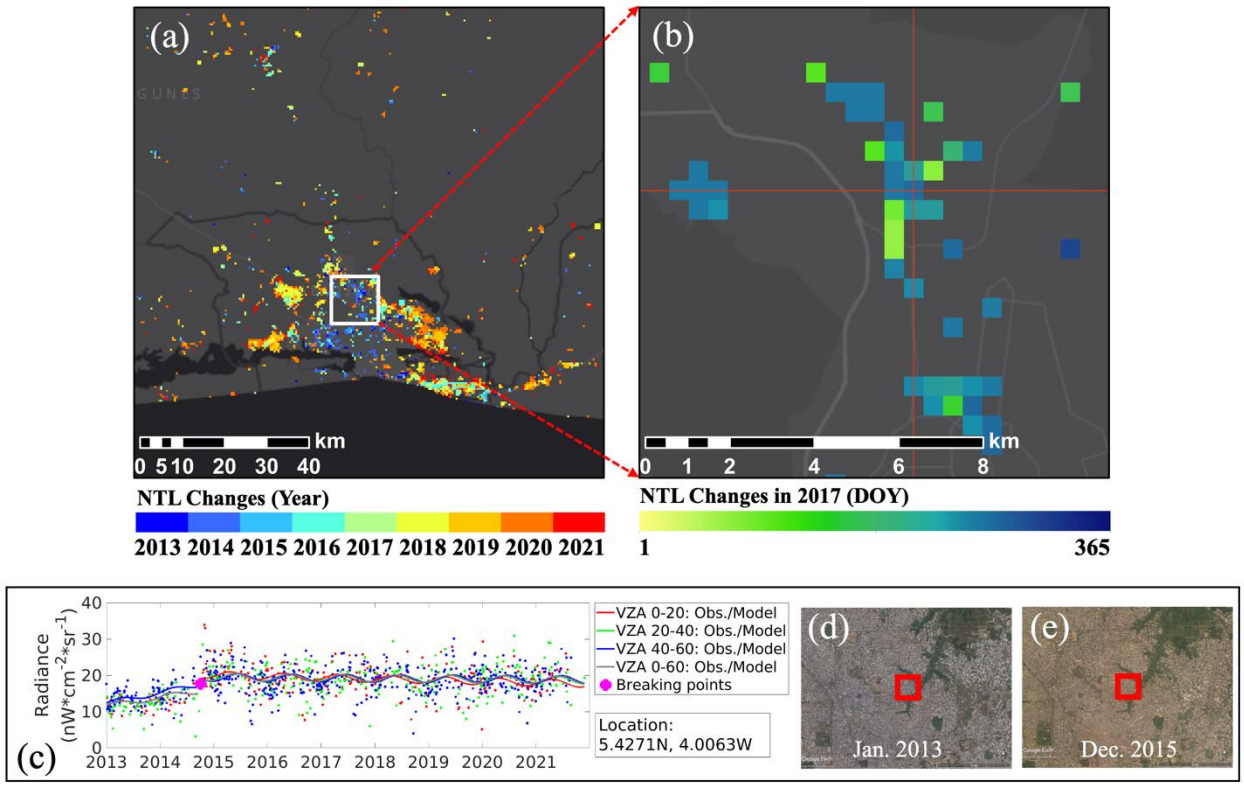

Fig. 13. The NTL change maps, the time series plot of a selected pixel, and high-resolution images for the city of Abidjan, Ivory Coast. (a) The accumulated annual NTL change maps from 2013 to 2021 with the latest detected change year presented. (b) The day-of-year NTL change map in 2014 over the region enlarged from the white rectangle from Fig. 13a. (c) The time series plot of a selected pixel (red cross in Fig. 13b) and the corresponding VZA-COLD detection results, in which the red, green, blue, and grey colors indicate the different VZA intervals, lines represent the estimated models, small dots are the DNB observations, and the large magenta dot is the detected changes. (d) The high-resolution Google Earth image in January 2013. The red rectangle represents the location and size of the selected pixel. (e) The high-resolution Google Earth image in December 2015. The red rectangle represents the location and size of the selected pixel. The dark background in Fig 13a and Fig. 13b is the Esri ArcMap Dark Gray Canvas base map.

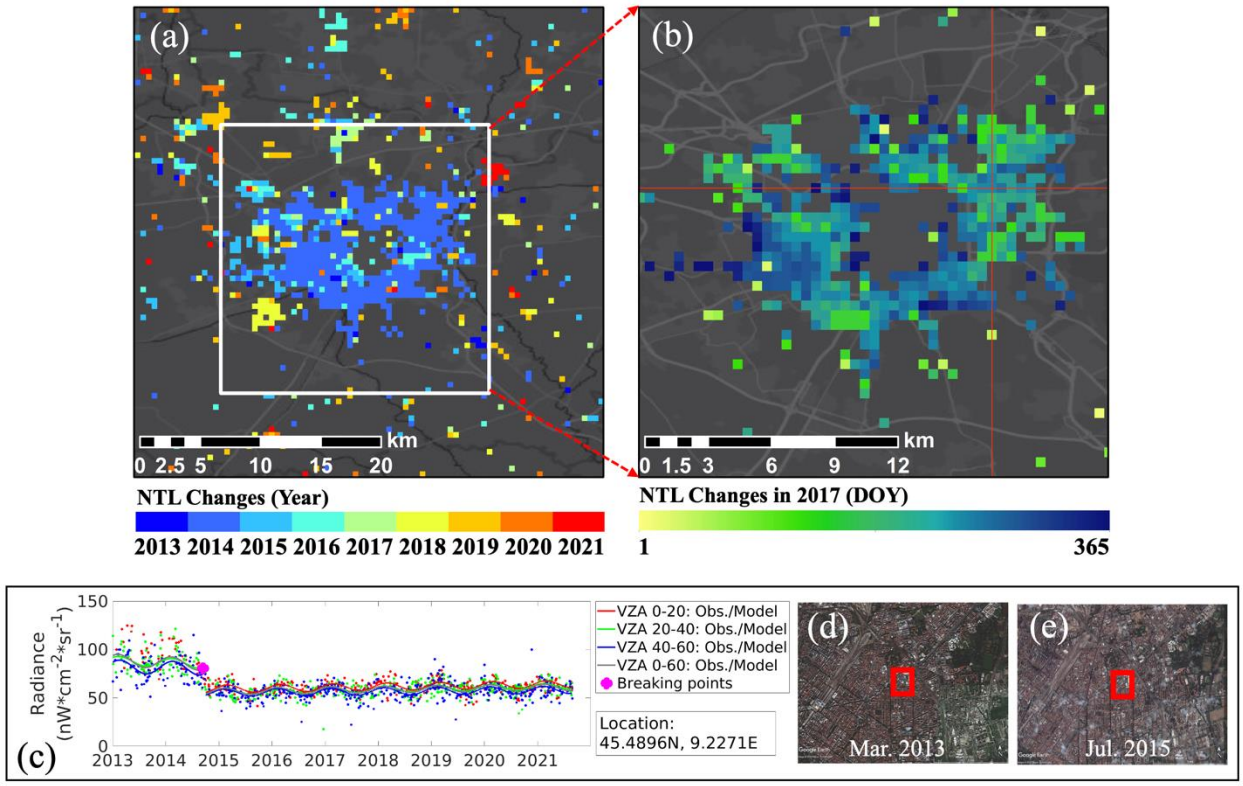

Fig. 14. The NTL change maps, the time series plot of a selected pixel, and high-resolution images for Milan, Italy. (a) The accumulated annual NTL change maps from 2013 to 2021 with the latest detected change year presented. (b) The day-of-year NTL change map in 2014 over the region enlarged from the white rectangle from Fig. 14a. (c) The time series plot of a selected pixel (red cross in Fig. 14b) and the corresponding VZA-COLD detection results, in which the red, green, blue, and grey colors indicate the different VZA intervals, lines represent the estimated models, small dots are the DNB observations, and the large magenta dot is the detected changes. (d) The high-resolution Google Earth image in March 2013. The red rectangle represents the location and size of the selected pixel. (e) The high-resolution Google Earth image in July 2015. The red rectangle represents the location and size of the selected pixel. The dark background in Fig. 14a and Fig. 14b is the Esri ArcMap Dark Gray Canvas base map.

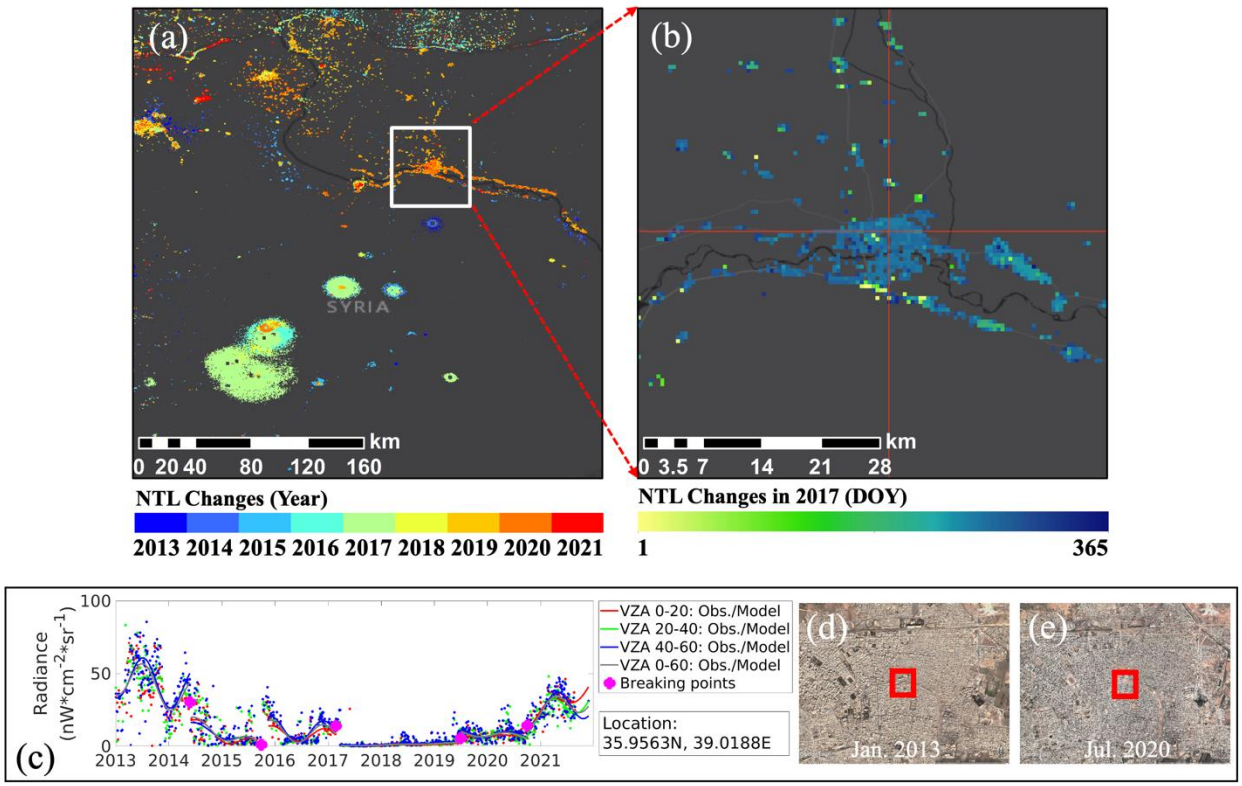

Fig. 15. The NTL change maps, the time series plot of a selected pixel, and high-resolution images for Raqqa, Syria. (a) The accumulated annual NTL change maps from 2013 to 2021 with the latest detected change year presented. (b) The day-of-year NTL change map in 2015 over the region enlarged from the white rectangle from Fig. 15a. (c) The time series plot of a selected pixel (red cross in Fig. 15b) and the corresponding VZA-COLD detection results, in which the red, green, blue, and grey colors indicate the different VZA intervals, lines represent the estimated models, small dots are the DNB observation, and the large magenta dots are the detected changes. (d) The high-resolution Google Earth image in January 2013. The red rectangle represents the location and size of the selected pixel. (e) The high-resolution Google Earth image in July 2020. The red rectangle represents the location and size of the selected pixel. The dark background in Fig. 15a and Fig. 15b is the Esri ArcMap Dark Gray Canvas base map.

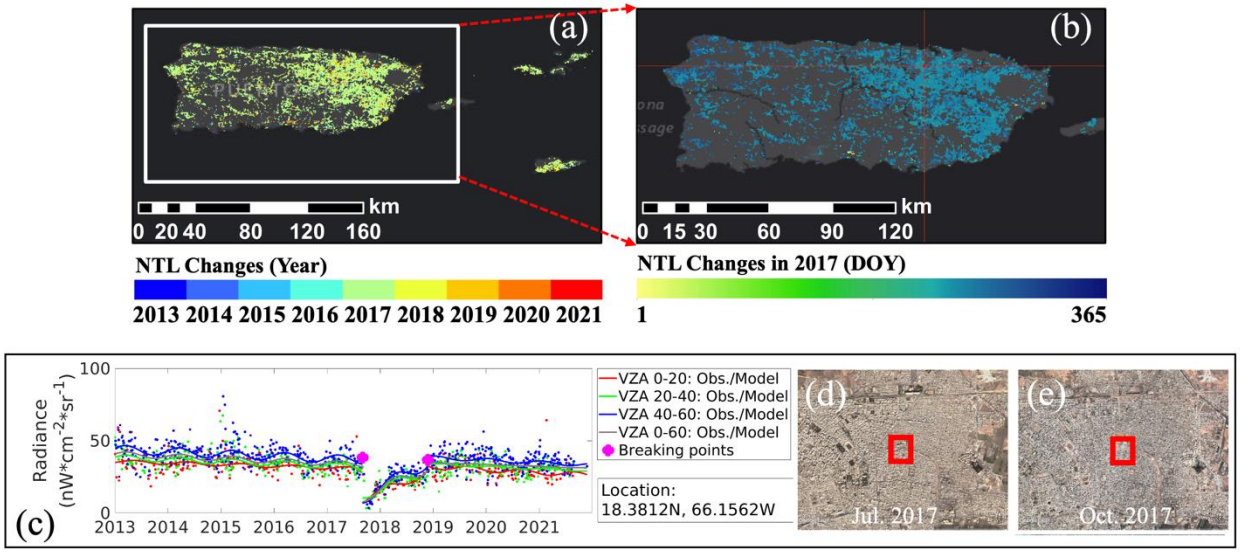

Fig. 16. The NTL change maps, the time series plot of a selected pixel, and high-resolution images for Puerto Rico. (a) The accumulated annual NTL change maps from 2013 to 2021 with the latest detected change year presented. (b) The day-of-day NTL change map in 2017 over the region enlarged from the white rectangle from Fig. 16a. (c) The time series plot of a selected pixel (red cross in Fig. 16b) and the corresponding VZA-COLD detection results, in which the red, green, blue, and grey colors indicate the different VZA intervals, lines represent the estimated models, small dots are the DNB observations, and the large magenta dots are the detected changes. (d) The high-resolution Google Earth image in July 2017. The red rectangle represents the location and size of the selected pixel. (e) The high-resolution Google Earth image in October 2017. The red rectangle represents the location and size of the selected pixel. The dark background in Fig. 16a and Fig. 16b is the Esri ArcMap Dark Gray Canvas base map.

4.2. Quantitative evaluation

Based on 1,088 stratified random samples and following the "good practice" (Olofsson et al., 2014), the overall accuracy of the map is 99.54%±0.19% (95% confidence interval), with a user's accuracy of 68.25%±3.40% (95% confidence interval) and producer's accuracy of 66.89%±16.19% (95% confidence interval) for the NTL change category.

5. Discussion and Conclusions

Understanding heterogeneity in human settlements is important for linking development patterns to ecological, economic, and social health (Stokes and Seto, 2019). While daytime optical remote

sensing has tracked urban land cover change for decades (Zhu et al., 2019), there is a need for new data and analytical tools to be able to monitor whether changes in urban infrastructure are keeping pace with key factors tied to global sustainability trends and opportunities. NTL data derived from the Suomi-NPP and NOAA-20 VIIRS DNB, have the potential to add our understanding of urban infrastructural transitions. But to date, the high temporal variation of the VIIRS DNB observations (Elvidge et al., 2022; Li et al., 2019; Wang et al., 2021) has made it challenging to monitor and detect these factors, at the characteristic temporal scales necessary to capture urban development processes. With the major environmental effects of atmosphere and moonlight removed, the atmospheric- and Lunar-BRDF-corrected NASA's Black Marble products provide new opportunities to use extremely dense (e.g., daily) NTL time series. In this study, we developed a VZA stratified algorithm for continuous monitoring of NTL changes based on the daily Black Marble products. With the observations stratified into four VZA intervals, this approach estimated an individual time series model for each VZA interval. Based on the predicted and the observed values, consistent breakpoints were identified and applied to all VZA stratified models as potential NTL changes when any of the VZA interval models detected consecutive anomaly observations (can tolerate one exception). Quantitative evaluation of the NTL change detection result showed that the algorithm can detect NTL changes with omission and commission error rates < 30%. In addition to the detected breakpoints of the NTL patterns, slopes of the estimated models can also provide extra information on the trend of gradual NTL radiances changes.

We developed new methods to filter, fit, and mitigate the high temporal uncertainties of the daily DNB time series observations. The applied 5x5 pixel buffer filtered potential outliers

surrounding cloud and snow pixels to mitigate the cloud and snow contamination. The single term harmonic model can estimate the intra-annual patterns of the DNB time series as a result of joint factors including vegetation phenology, winter snow coverage, and cyclical human activity changes. We mitigated and simplified the complex and combined effects of the wide ranges of sensor viewing angle and different surface geometry conditions by stratifying the DNB time series based on four sets of VZA intervals. Compared with correcting the viewing angle effect (Tan et al., 2022), the stratification strategy avoided the need for collecting local 3-dimensional structure data and would not be influenced by the potential bias introduced in the correction approaches. The combined knowledge derived from VZA interval subsets, and all data models reduced the variance across VZAs without decreasing the temporal frequency of the data. This new VZA stratification approach would be particularly useful for pixels with strong angular effects and changes that can only be observed under specific viewing angles. For pixels with homogeneous emission among different viewing angles and short-term NTL changes, all data models with 0-60 VZAs could provide accurate and timely results.

The VZA-COLD algorithm can accurately detect different types of human-related NTL changes, either with or without land cover conversion (e.g., urban expansion). For NTL changes with land cover conversion, the concurrent changes of urbanization processes, construction actions, and land cultivation can be well detected with the potential in providing additional information about the land cover conversion stages. For the NTL changes without land cover conversion, the algorithm can identify the long-term and short-term land cover condition change, such as de-electrification of the electric infrastructure, electric grid variations, and human behavior related disturbances. Compared with the daytime optical remote sensing imagery, the NTL change

metrics can provide complementary information of the human activity patterns that do not necessarily cause changes in land cover and provide a better understanding of coupling human-environment systems with a unique perspective.

Although VZA-COLD can model and detect the abrupt, cyclical, and gradual NTL changes for both the view angle affected and unaffected regions, it also has some limitations. For example, high latitude areas with large coverage of winter snow/ice could still lead to many commission errors if the cloud/snow QA and their buffers did not exclude them well. This error could be reduced in the upcoming Collection 2 Black Marble products after reprocessing all the data with an improved snow flag derived from the VIIRS snow product with higher spatial resolution. Moreover, the change probability threshold for each time series model is currently calculated based on the same RMSE for all periods, and the temporally varying fluctuations caused by the winter weather are more likely to be identified as NTL changes. To overcome this issue, further adjustments could be performed to consider the changing temporal variation of NTL data within a year, such as applying the temporally adjusted RMSE values for change detection (Zhu et al., 2015). Moreover, further post-processing steps such as filtering or including NTL changes based on their spatial patterns could also be explored.

In conclusion, we developed a VZA stratified COLD algorithm to continuously monitor NTL changes based on the daily atmospheric- and Lunar-BRDF-corrected Black Marble product. This method enabled the dense daily time series analysis of the DNB data by reducing the viewing angle introduced variations without decreasing the temporal frequency of the data. The results

589 indicate that this method could be applied for operational mapping of global NTL changes at a
590 spatial resolution of 15-arc-second with a daily updating frequency.
591
592 **Acknowledgment**
593 This work was supported by NASA's Terra, Aqua, Suomi-NPP, and NOAA-20 program grant
594 80NSSC22K0199, and is based upon work supported in part by the Office of the Director of
595 National Intelligence (ODNI), Intelligence Advanced Research Projects Activity (IARPA), via
596 2021-2011000005. The U.S. Government is authorized to reproduce and distribute reprints for
597 Governmental purposes notwithstanding any copyright annotation thereon. Disclaimer: The
598 views and conclusions contained herein are those of the authors and should not be interpreted as
599 necessarily representing the official policies or endorsements, either expressed or implied, of
600 ODNI, IARPA, or the U.S. Government. The U.S. Government is authorized to reproduce and
601 distribute reprints for governmental purposes notwithstanding any copyright annotation therein.
602
603 **References**
604 Baumann, M., Kuemmerle, T., 2016. The impacts of warfare and armed conflict on land systems.
605 J. Land Use Sci. 11, 672–688.
606 https://doi.org/https://doi.org/10.1080/1747423X.2016.1241317
607 Chen, Z., Yu, B., Zhou, Y., Liu, H., Yang, C., Shi, K., Wu, J., 2019. Mapping Global Urban
608 Areas from 2000 to 2012 Using Time-Series Nighttime Light Data and MODIS Products.
609 IEEE J. Sel. Top. Appl. Earth Obs. Remote Sens. 12, 1143–1153.
610 https://doi.org/10.1109/JSTARS.2019.2900457
611 Coesfeld, J., Anderson, S.J., Baugh, K., Elvidge, C.D., Schernthanner, H., Kyba, C.C.M., 2018.

612 Variation of Individual Location Radiance in VIIRS DNB Monthly Composite Images.
613 Remote Sens. 10, 1964. https://doi.org/10.3390/RS10121964
614 Deng, J.S., Wang, K., Hong, Y., Qi, J.G., 2009. Spatio-temporal dynamics and evolution of land
615 use change and landscape pattern in response to rapid urbanization. Landsc. Urban Plan. 92,
616 187–198. https://doi.org/10.1016/J.LANDURBPLAN.2009.05.001
617 Elvidge, C.D., Baugh, K., Zhizhin, M., Hsu, F.C., Ghosh, T., 2017. VIIRS night-time lights. Int.
618 J. Remote Sens. 38, 5860–5879. https://doi.org/10.1080/01431161.2017.1342050
619 Elvidge, C.D., Baugh, K.E., Hobson, V.R., Kihn, E.A., Kroehl, H.W., Davis, E.R., Cocero, D.,
620 1997. Satellite inventory of human settlements using nocturnal radiation emissions: a
621 contribution for the global toolchest. Glob. Chang. Biol. 3, 387–395.
622 https://doi.org/10.1046/J.1365-2486.1997.00115.X
623 Elvidge, C.D., Zhizhin, M., Ghosh, T., Hsu, F.C., Taneja, J., 2021. Annual Time Series of Global
624 VIIRS Nighttime Lights Derived from Monthly Averages: 2012 to 2019. Remote Sens. 13,
625 922. https://doi.org/10.3390/RS13050922
626 Elvidge, C.D., Zhizhin, M., Keith, D., Miller, S.D., Hsu, F.C., Ghosh, T., Anderson, S.J.,
627 Monrad, C.K., Bazilian, M., Taneja, J., Sutton, P.C., Barentine, J., Kowalik, W.S., Kyba,
628 C.C.M., Pack, D.W., Hammerling, D., 2022. The VIIRS Day/Night Band: A Flicker Meter
629 in Space? Remote Sens. 14, 1316. https://doi.org/10.3390/RS14061316
630 Green, J., Perkins, C., Steinbach, R., Edwards, P., 2015. Reduced street lighting at night and
631 health: A rapid appraisal of public views in England and Wales. Health Place 34, 171–180.
632 https://doi.org/10.1016/J.HEALTHPLACE.2015.05.011
633 Hampel, F.R., Ronchetti, E.M., Rousseeuw, P.J., Stahel, W.A., 2011. Robust statistics: the
634 approach based on influence functions. John Wiley & Sons.

635 Hölker, F., Moss, T., Griefahn, B., Kloas, W., Voigt, C.C., Henckel, D., Hänel, A., Kappeler,
636 P.M., Völker, S., Schwope, A., 2010. The dark side of light: a transdisciplinary research
637 agenda for light pollution policy. Ecol. Soc. 15.
638 Jensen, J.R., Cowen, D.C., 1999. Remote sensing of urban/suburban infrastructure and socio-
639 economic attributes. Photogramm. Eng. Remote Sensing 65, 611–622.
640 Leu, J., Yen, I.H., Gansky, S.A., Walton, E., Adler, N.E., Takeuchi, D.T., 2008. The association
641 between subjective social status and mental health among Asian immigrants: Investigating
642 the influence of age at immigration. Soc. Sci. Med. 66, 1152–1164.
643 https://doi.org/10.1016/J.SOCSCIMED.2007.11.028
644 Levin, N., 2017. The impact of seasonal changes on observed nighttime brightness from 2014 to
645 2015 monthly VIIRS DNB composites. Remote Sens. Environ. 193, 150–164.
646 https://doi.org/10.1016/j.rse.2017.03.003
647 Levin, N., Kyba, C.C.M., Zhang, Q., Sánchez de Miguel, A., Román, M.O., Li, X., Portnov,
648 B.A., Molthan, A.L., Jechow, A., Miller, S.D., Wang, Z., Shrestha, R.M., Elvidge, C.D.,
649 2020. Remote sensing of night lights: A review and an outlook for the future. Remote Sens.
650 Environ. 237. https://doi.org/10.1016/j.rse.2019.111443
651 Li, X., Levin, N., Xie, J., Li, D., 2020. Monitoring hourly night-time light by an unmanned aerial
652 vehicle and its implications to satellite remote sensing. Remote Sens. Environ. 247, 111942.
653 https://doi.org/10.1016/j.rse.2020.111942
654 Li, X., Liu, S., Jendryke, M., Li, D., Wu, C., 2018. Night-Time Light Dynamics during the Iraqi
655 Civil War. Remote Sens. 10, 858. https://doi.org/10.3390/RS10060858
656 Li, X., Ma, R., Zhang, Q., Li, D., Liu, S., He, T., Zhao, L., 2019. Anisotropic characteristic of
657 artificial light at night – Systematic investigation with VIIRS DNB multi-temporal

observations. Remote Sens. Environ. 233. https://doi.org/10.1016/j.rse.2019.111357

Li, X., Shang, X., Zhang, Q., Li, D., Chen, F., Jia, M., Wang, Y., 2022. Using radiant intensity to characterize the anisotropy of satellite-derived city light at night. Remote Sens. Environ. 271, 112920. https://doi.org/10.1016/J.RSE.2022.112920

Liu, S., Li, X., Levin, N., Jendryke, M., 2019. Tracing cultural festival patterns using time-series of VIIRS monthly products. Remote Sens. Lett. 10, 1172–1181. https://doi.org/10.1080/2150704X.2019.1666313

Ma, T., Zhou, C., Pei, T., Haynie, S., Fan, J., 2012. Quantitative estimation of urbanization dynamics using time series of DMSP/OLS nighttime light data: A comparative case study from China's cities. Remote Sens. Environ. 124, 99–107. https://doi.org/10.1016/J.RSE.2012.04.018

Machlis, G.E., Román, M.O., Pickett, S.T.A., 2022. A framework for research on recurrent acute disasters. Sci. Adv. 8, 2458. https://doi.org/10.1126/SCIADV.ABK2458

Malecki, E.J., 1997. Technology and economic development: the dynamics of local, regional, and national change. Univ. Illinois Urbana-Champaign's Acad. Entrep. Leadersh. Hist. Res. Ref. Entrep.

Ojima, D.S., Galvin, K.A., Turner, B.L.I.I., 1994. The global impact of land-use change. Bioscience 44, 300–304. https://doi.org/10.2307/1312379

Olofsson, P., Foody, G.M., Herold, M., Stehman, S. V., Woodcock, C.E., Wulder, M.A., 2014. Good practices for estimating area and assessing accuracy of land change. Remote Sens. Environ. 148, 42–57. https://doi.org/10.1016/j.rse.2014.02.015

Ramiaramanana, F.N., Lam, K., Martinez, L., 2021. Policy making and political implications and contradictions in changing urban environment-Housing and public transport in Abidjan,

Ivory Coast.

Román, M.O., Stokes, E.C., 2015. Holidays in lights: Tracking cultural patterns in demand for energy services. Earth's Futur. 3, 182–205. https://doi.org/10.1002/2014EF000285

Román, M.O., Stokes, E.C., Shrestha, R., Wang, Z., Schultz, L., Carlo, E.A.S., Sun, Q., Bell, J., Molthan, A., Kalb, V., Ji, C., Seto, K.C., McClain, S.N., Enenkel, M., 2019. Satellite-based assessment of electricity restoration efforts in Puerto Rico after Hurricane Maria. PLoS One 14, e0218883. https://doi.org/10.1371/journal.pone.0218883

Román, M.O., Wang, Z., Sun, Q., Kalb, V., Miller, S.D., Molthan, A., Schultz, L., Bell, J., Stokes, E.C., Pandey, B., Seto, K.C., Hall, D., Oda, T., Wolfe, R.E., Lin, G., Golpayegani, N., Devadiga, S., Davidson, C., Sarkar, S., Praderas, C., Schmaltz, J., Boller, R., Stevens, J., Ramos González, O.M., Padilla, E., Alonso, J., Detrés, Y., Armstrong, R., Miranda, I., Conte, Y., Marrero, N., MacManus, K., Esch, T., Masuoka, E.J., 2018. NASA's Black Marble nighttime lights product suite. Remote Sens. Environ. 210, 113–143. https://doi.org/10.1016/j.rse.2018.03.017

Shi, K., Huang, C., Yu, B., Yin, B., Huang, Y., Wu, J., 2014. Evaluation of NPP-VIIRS night-time light composite data for extracting built-up urban areas. Remote Sens. Lett. 5, 358–366. https://doi.org/10.1080/2150704X.2014.905728

Steffen, W., Sanderson, R.A., Tyson, P.D., Jäger, J., Matson, P.A., Moore III, B., Oldfield, F., Richardson, K., Schellnhuber, H.-J., Turner, B.L., 2006. Global change and the earth system: a planet under pressure. Springer Science & Business Media.

Stokes, E.C., Seto, K.C., 2019. Characterizing urban infrastructural transitions for the Sustainable Development Goals using multi-temporal land, population, and nighttime light data. Remote Sens. Environ. 234, 111430. https://doi.org/10.1016/J.RSE.2019.111430

Tan, X., Zhu, X., Chen, J., Chen, R., 2022. Modeling the direction and magnitude of angular effects in nighttime light remote sensing. Remote Sens. Environ. 269, 112834. https://doi.org/10.1016/J.RSE.2021.112834

Tang, Y., Shao, Z., Huang, X., Cai, B., 2021. Mapping Impervious Surface Areas Using Time-Series Nighttime Light and MODIS Imagery. Remote Sens. 13, 1900. https://doi.org/10.3390/RS13101900

Tibshiranit, R., 1996. Regression Shrinkage and Selection Via the Lasso. J. R. Stat. Soc. Ser. B 58, 267–288. https://doi.org/10.1111/J.2517-6161.1996.TB02080.X

Turner, M.G., 2010. Disturbance and landscape dynamics in a changing world. Ecology 91, 2833–2849. https://doi.org/10.1890/10-0097.1

Venter, O., Sanderson, E.W., Magrach, A., Allan, J.R., Beher, J., Jones, K.R., Possingham, H.P., Laurance, W.F., Wood, P., Fekete, B.M., Levy, M.A., Watson, J.E.M., 2016. Global terrestrial Human Footprint maps for 1993 and 2009. Sci. Data 2016 31 3, 1–10. https://doi.org/10.1038/sdata.2016.67

Wang, Z., Román, M.O., Kalb, V.L., Miller, S.D., Zhang, J., Shrestha, R.M., 2021. Quantifying uncertainties in nighttime light retrievals from Suomi-NPP and NOAA-20 VIIRS Day/Night Band data. Remote Sens. Environ. 263, 112557. https://doi.org/10.1016/J.RSE.2021.112557

Xie, Y., Weng, Q., 2016. Updating urban extents with nighttime light imagery by using an object-based thresholding method. Remote Sens. Environ. 187, 1–13. https://doi.org/10.1016/J.RSE.2016.10.002

Xie, Y., Weng, Q., Fu, P., 2019. Temporal variations of artificial nighttime lights and their implications for urbanization in the conterminous United States, 2013–2017. Remote Sens. Environ. 225, 160–174. https://doi.org/10.1016/j.rse.2019.03.008

727 Yang, D., Luan, W., Qiao, L., Pratama, M., 2020. Modeling and spatio-temporal analysis of city-
728 level carbon emissions based on nighttime light satellite imagery. Appl. Energy 268,
729 114696. https://doi.org/10.1016/J.APENERGY.2020.114696
730 Yu, B., Shi, K., Hu, Y., Huang, C., Chen, Z., Wu, J., 2015. Poverty Evaluation Using NPP-
731 VIIRS Nighttime Light Composite Data at the County Level in China. IEEE J. Sel. Top.
732 Appl. Earth Obs. Remote Sens. 8, 1217–1229.
733 https://doi.org/10.1109/JSTARS.2015.2399416
734 Zhang, Q., Seto, K.C., 2011. Mapping urbanization dynamics at regional and global scales using
735 multi-temporal DMSP/OLS nighttime light data. Remote Sens. Environ. 115, 2320–2329.
736 https://doi.org/10.1016/j.rse.2011.04.032
737 Zhao, N., Liu, Y., Hsu, F.C., Samson, E.L., Letu, H., Liang, D., Cao, G., 2020. Time series
738 analysis of VIIRS-DNB nighttime lights imagery for change detection in urban areas: A
739 case study of devastation in Puerto Rico from hurricanes Irma and Maria. Appl. Geogr. 120,
740 102222. https://doi.org/10.1016/j.apgeog.2020.102222
741 Zheng, Q., Weng, Q., Wang, K., 2021. Characterizing urban land changes of 30 global
742 megacities using nighttime light time series stacks. ISPRS J. Photogramm. Remote Sens.
743 173, 10–23. https://doi.org/10.1016/J.ISPRSJPRS.2021.01.002
744 Zhu, Z., Woodcock, C.E., Holden, C., Yang, Z., 2015. Generating synthetic Landsat images
745 based on all available Landsat data: Predicting Landsat surface reflectance at any given
746 time. Remote Sens. Environ. 162, 67–83. https://doi.org/10.1016/J.RSE.2015.02.009
747 Zhu, Z., Woodcock, C.E., Rogan, J., Kellndorfer, J., 2012. Assessment of spectral, polarimetric,
748 temporal, and spatial dimensions for urban and peri-urban land cover classification using
749 Landsat and SAR data. Remote Sens. Environ. 117, 72–82.

https://doi.org/10.1016/j.rse.2011.07.020

Zhu, Z., Zhang, J., Yang, Z., Aljaddani, A.H., Cohen, W.B., Qiu, S., Zhou, C., 2020. Continuous monitoring of land disturbance based on Landsat time series. Remote Sens. Environ. 238, 111116. https://doi.org/10.1016/j.rse.2019.03.009

Zhu, Z., Zhou, Y., Seto, K.C., Stokes, E.C., Deng, C., Pickett, S.T.A., Taubenböck, H., 2019. Understanding an urbanizing planet: Strategic directions for remote sensing. Remote Sens. Environ. 228, 164–182. https://doi.org/10.1016/J.RSE.2019.04.020